

Carbon dissolution and diffusion in ferrite and austenite from first principles

D. E. Jiang and Emily A. Carter

Department of Chemistry and Biochemistry, Box 951569, University of California, Los Angeles, California 90095-1569, USA

(Received 19 February 2003; published 19 June 2003)

We perform density-functional theory (DFT) calculations of carbon dissolution and diffusion in iron, the latter being a typical example of interstitial diffusion. The Kohn-Sham equations are solved with periodic boundary conditions and within the projector-augmented-wave formalism, using the generalized gradient approximation for electron exchange and correlation. With the solution enthalpy as an indication of cell size convergence, we find a supercell with 128 Fe atoms and one C atom is sufficient for describing dilute concentrations of carbon in bcc Fe. The solution enthalpy of carbon in an octahedral site in ferrite is predicted to be 0.74 eV, i.e., the dissolution of carbon in bcc ferromagnetic (FM) Fe is an endothermic process. Using the Fe128C1 periodic cell, we find that the minimum-energy path (MEP) of carbon diffusion from one octahedral site to another (via a tetrahedral site) has a barrier of 0.86 eV, in excellent agreement with the experimental value of 0.87 eV. This encouraging benchmark result prompted us to investigate carbon diffusion in austenite, whose electronic structure is less well characterized experimentally. Cell size convergence results show that a supercell with 32 Fe atoms and one C atom is sufficient. The calculated solution enthalpy is -0.17 eV, which indicates that the dissolution of carbon in fcc Fe is exothermic, consistent with the known greater solubility of C in austenite compared to ferrite. The MEP shows that carbon moves linearly from an octahedral site to another, contrary to the common notion of an off-plane diffusion path. The diffusion barrier is calculated to be 0.99 eV. Since we model austenite with the FM high-spin phase, the diffusion barrier we obtain is not directly comparable to the experiments in which austenite is usually paramagnetic. However, this prediction is relevant for C incorporation into Fe thin films, since FM high-spin fcc Fe can be obtained by epitaxial growth of thin Fe films on a Cu substrate.

DOI: 10.1103/PhysRevB.67.214103

PACS number(s): 66.30.Jt, 71.15.Mb, 71.15.Nc

I. INTRODUCTION

Many important phenomena in materials science involve diffusion of impurities. Diffusion of the light elements (H, B, C, N, and O) in metals typically occurs via an interstitial mechanism. One example is carbon diffusion in iron. Due to its relatively high diffusivity, interstitial diffusion of carbon often controls the kinetics of phase transformations in steels and therefore the resulting microstructure. Moreover, some technologically important processes such as surface hardening by carburizing and nitriding are realized by interstitial diffusion. Molecule-surface interactions, such as those in corrosion and heterogeneous catalysis, can also involve diffusion of adsorbed atoms into subsurface layers and further into the bulk. However, interstitial diffusion may cause problems such as strain aging, embrittlement, and steel erosion. Understanding the interstitial diffusion process in iron may aid in understanding the behavior of steel subject to harsh environments.

Despite more than 50 years of experiments investigating carbon diffusion in ferrite [body-centered-cubic (bcc) Fe and its carbon alloy, also called the α phase] and austenite [face-centered-cubic (fcc) Fe and its carbon alloy, also called the γ phase], some key issues remain unclear. For instance, direct evidence of the diffusion path is still lacking due to inherent limitations in spatial and time resolution of experimental techniques that do not permit probing of individual reactive events in solids (not to mention the difficulty associated with probing a transition state in condensed matter). Periodic density-functional theory^{1,2} coupled with a solid-state transition-state search algorithm provides a way to study the

atomic mechanism of solid-state diffusion. The success of several such studies³⁻⁶ encourages us to work on carbon diffusion in iron which, to our knowledge, has not been studied by first principles before. We have chosen carbon diffusion in Fe as our starting point because it has broad industrial applications and accurate experimental data are available. In addition, carbon diffusion in Fe is a very typical case and the knowledge from that may offer a general picture of interstitial diffusion of elements in bcc and fcc metals.

The classical measurement of carbon diffusion in ferrite in 1950 by Wert⁷ showed that in the temperature range of 238–473 K, the data agree very well with a linear Arrhenius plot which yields a diffusion barrier of 0.87 eV. After Wert, carbon diffusion in ferrite was measured with various methods and in different temperature ranges.⁸ For the low-temperature linear Arrhenius regime, the atomic mechanism assumed by many⁸⁻¹² involves carbon movement from the octahedral (o) site to another nearest-neighbor o-site via the tetrahedral (t) site, with the t-site assumed to be the transition state (TS).

The measurement of carbon diffusion in austenite also started in the 1950s. Wells *et al.*¹³ and Smith¹⁴ showed that at 0.1-wt % concentration of carbon in austenite, the diffusion barrier is about 1.60 eV. Although the solubility of carbon in austenite is high and high-resolution neutron powder-diffraction experiments indicate^{15,16} that carbon resides in the o-site of the lattice, the atomic level diffusion pathway is still unclear.

Due to the very low solubility of carbon in ferrite (0.022 wt % at about 1000 K), a realistic study of atomic diffusion is challenging with first-principles techniques. By building a

large Fe cell with one C atom in it and periodically repeating the cell in all three dimensions, the supercell approximation allows us to solve this problem to a certain degree. Here, we first calculate the solution enthalpy of carbon in bcc and fcc Fe and examine how the enthalpy converges with the size of the supercell. After a suitable supercell is obtained, we then go on to find the minimum-energy path (MEP) for carbon diffusion and the associated energy barriers in both bcc and fcc Fe. Our objective is to test the assumed pathway for bcc Fe and to attempt to predict the preferred pathway in fcc Fe.

The rest of the paper is organized as follows. Section II describes the method we use, in Sec. III we present the results, Sec. IV discusses some issues relating our findings to experiments, and Sec. V summarizes the results and gives conclusions.

II. METHOD

The first-principles calculations performed in this study are based on spin-polarized density-functional theory (DFT).^{17,18} The Vienna *ab initio* simulation package (VASP, version 4.4.5) is used to solve the Kohn-Sham equations^{19–21} with periodic boundary conditions and a plane-wave basis set. Here we employ Blöchl’s projector-augmented-wave (PAW) method²² as implemented by Kresse and Joubert.²³ The PAW method is an all-electron DFT technique (within the frozen-core approximation) with the computational efficiency of pseudopotential DFT algorithms. Its use is necessary for accurate calculations of certain transition metals, which are sometimes poorly described by ultrasoft pseudopotentials.²⁴ For the treatment of electron exchange and correlation, it is well known that the generalized gradient approximation (GGA) is needed to give an accurate description of magnetic properties and energetics of Fe bulk phases.²⁵ Therefore all calculations are done with the GGA functional of Perdew *et al.*²⁶ using the one-electron quantities (partial waves, projectors, etc.) supplied with VASP that are required to construct the self-consistent PAW potentials. (We use the standard version of the PAW-GGA potential for Fe and the soft one for C.) The spin interpolation of the correlation energy is by the Vosko-Wilk-Nusair method.²⁷ The equation of state (energy versus volume) for bulk Fe is fit to Murnaghan’s equation of state.²⁹ The equilibrium volumes (and thus, the lattice parameters) and bulk moduli are extracted from the fit.

When the number of atoms in a supercell exceeds 20, the projection operators in the PAW method are evaluated in real space to aid computational efficiency. We use a kinetic-energy cutoff of 350 eV, which we find is sufficient to converge the total energies of graphite and ferromagnetic (FM) bcc Fe to within 5 meV/atom. We find that a 350-eV kinetic-energy cutoff converges the solution enthalpy (for carbon in the octahedral site of an unrelaxed bcc Fe16 supercell) to within 6 meV per carbon atom. The Monkhorst-Pack scheme²⁸ is used for the k -point sampling, and for each supercell, the total energy is converged with respect to k -point sampling to within 0.02 eV/cell (Table I lists the k -point mesh used for each supercell). The first-order Methfessel-Paxton method is used for Fermi-surface smearing in order

TABLE I. Converged k -point meshes used for the bcc and fcc Fe supercells.

bcc	k -mesh	fcc	k -mesh
Fe16	$8 \times 8 \times 8$	Fe4	$8 \times 8 \times 8$
Fe54	$6 \times 6 \times 6$	Fe32	$6 \times 6 \times 6$
Fe128	$4 \times 4 \times 4$	Fe64	$4 \times 4 \times 4$
		Fe125	$2 \times 2 \times 2$

to obtain accurate forces,²¹ and the smearing width is chosen such that the error in the energy extrapolated to 0 K is less than 1 meV/atom (we use a smearing width of 0.05 eV for bcc Fe125 and fcc Fe128 supercells and 0.1 eV for all the other cells). When the maximum force acting on each atom of the supercell drops below 0.005 eV/Å, the structural relaxation is terminated. For carbon in bcc Fe, we first use the conjugate-gradient method for ionic relaxation for 20 steps, and then a quasi-Newton method subsequently for approximately five ionic iterations to reach the prescribed force tolerance. For carbon in fcc Fe, the direct use of the quasi-Newton method can usually converge the structure within ten ionic iterations.

The solution enthalpy at 0 K, neglecting zero-point energy corrections (later, we show these are small), of carbon in an Fe bulk lattice is defined as the following:

$$\Delta H_s = E(\text{Fe}_n\text{C}_1) - E(\text{Fe}_n) - E(\text{C}). \quad (1)$$

The first term on the right-hand side is the total energy of the supercell that includes n Fe atoms and one carbon atom; the second term is the total energy of the supercell that consists of n Fe atoms. The first two terms are calculated with the same parameters (k -point sampling, kinetic-energy cutoff, etc.) as given above. The third term is the total energy of graphite on a per atom basis and is calculated separately with respect to k -point convergence. Since the van der Waals interaction between graphite sheets is not described properly with DFT GGA, we model graphite using the experimental geometry [$a = 2.462$ Å and $c = 6.656$ Å at 0 K (Ref. 30)] and do not optimize its structure. We calculate the total energy of graphite with a kinetic-energy cutoff of 350 eV and a $8 \times 8 \times 4$ k -mesh. We obtain a cohesive energy of $E_{coh} = 8.01$ eV/atom for graphite (with respect to the ³P ground state of atomic C) that exceeds the experimental value³¹ by 0.64 eV, but is consistent with the typical error in DFT predictions of cohesive energies (LDA overestimates E_{coh} by 1.3 eV/atom for graphite³³).

An improved version of the nudged elastic Band (NEB) method, the climbing-image NEB,³⁴ is used to locate MEP’s and TS’s for the diffusion of carbon in bulk Fe. The NEB method³⁵ provides the means to find an MEP given the initial and final states of a process. An interpolated chain of configurations (images) between the initial and final positions are connected by springs and are relaxed simultaneously. With appropriate projections, the true force and the spring force acting on each image are separated from the total force. The true force relaxes the image to an MEP and the spring force keeps images with equal distance. With the climbing-

image scheme, the highest-energy image climbs uphill to the saddle point by making the spring force zero and including only the inverted parallel component of the true force on that image. When we use the climbing-image-NEB (CI-NEB) method in this study, all the images are relaxed until the maximum force acting on an atom is less than 0.01 eV/\AA . A velocity quench algorithm³⁶ is used for ionic relaxation to partially converge the images, followed by a quasi-Newton algorithm. All saddle points are then verified to be true transition states (rank 1 saddle points) and intermediates to be local minima by diagonalizing a finite difference construction of the Hessian matrix with displacements of 0.01 \AA and ensuring the presence of only one negative eigenvalue for TS's and all positive eigenvalues for minima.

For carbon diffusion in bcc Fe, a supercell of Fe128C1 is used for the CI-NEB calculation. Seven linearly interpolated images are converged to the MEP with a $2 \times 2 \times 2$ mesh for k -point sampling within approximately 30 ionic steps. For carbon diffusion in fcc Fe, our initial guess is a slightly perturbed set of linear interpolation images between the initial and final states with 15 images for a Fe4C1 cell ($6 \times 6 \times 6$ k -mesh) and 11 images for a Fe32C1 cell ($4 \times 4 \times 4$ k -mesh). The initial guesses converge to the MEP within approximately 60 ionic iterations for carbon diffusion in fcc Fe. Although we use a smaller k -mesh for Fe4C1, Fe32C1, and Fe128C1 cells for CI-NEB calculations compared with the solution enthalpy calculations, we find that a larger k -mesh changes the diffusion barriers by less than 0.02 eV .

III. RESULTS

A. Bulk Fe

Due to the four unpaired valence electrons of its atom, Fe in its various forms (clusters, surfaces, thin films, and bulk) shows very rich magnetic phenomena. Many first-principles studies successfully described the magnetic phases of bulk and thin-film Fe.^{37–41} A number of earlier calculations employed the all-electron full potential linearized augmented plane-wave (FLAPW) DFT method. As first realized by Blöchl,²² the PAW and FLAPW methods are closely connected, and Kresse and Joubert²³ have already demonstrated agreement between FLAPW and PAW DFT for some bulk Fe properties. However, a detailed study of the various magnetic phases of fcc Fe has not been reported using the PAW method, so we present one here, along with that for bcc Fe. This is necessary in order to choose a suitable magnetic phase to model ferrite and austenite.

The equations of state for FM, antiferromagnetic (AFM), and nonmagnetic (NM) bcc and fcc Fe are shown in Fig. 1. The lattice parameters, bulk moduli, and local magnetic moments for different magnetic phases of bcc and fcc Fe are listed in Table II, and compared with the FLAPW-DFT-GGA predictions and with experiment. The antiferromagnetic single-layer (AFM1) and antiferromagnetic double-layer (AFMD) phases (after Herper *et al.*⁴⁰) refer to the common antiferromagnetic structure ($\uparrow\downarrow\uparrow\downarrow \dots$) and the bilayer AFM structure ($\uparrow\uparrow\downarrow\downarrow \dots$), respectively. Both AFM phases have a [001] layer orientation, but the AFM1 phase has one layer spin up and the next layer spin down, while the AFMD phase

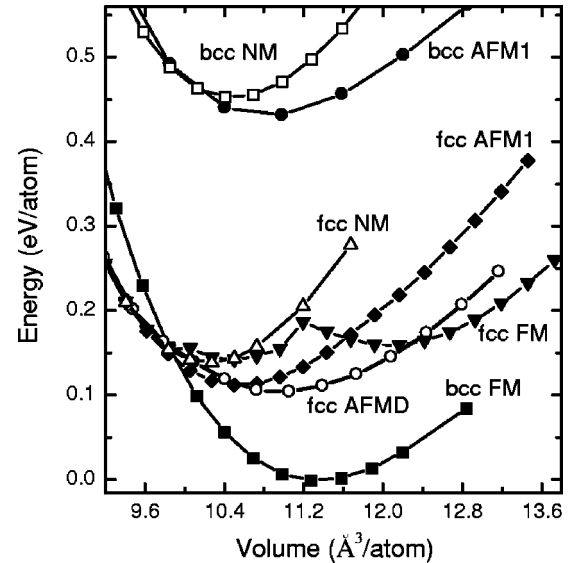


FIG. 1. Phase diagram for bcc Fe and fcc Fe with different magnetic configurations.

has two layers spin up and the next two layers spin down. In general, our results agree very well with the all-electron FLAPW-GGA results of Herper *et al.*⁴⁰ We obtain the FM bcc phase as the ground state of bulk Fe, as observed experimentally, so it is straightforward for us to choose the FM bcc phase as the model system for carbon diffusion in ferrite. Moreover, PAW-DFT GGA yields bulk properties for FM bcc Fe in good agreement with experiment (Table II).

The situation with austenite is not nearly so simple. Experiments suggest⁴⁴ that the ground state of fcc Fe is a spin-spiral state, which has been confirmed with first-principles noncollinear-spin calculations.^{45,46} We obtain the AFMD phase as the ground state of fcc Fe, which agrees with FLAPW results; the predicted lattice parameter for the AFMD state coincides reasonably with those extrapolated from measured lattice parameters in AFM fcc Fe alloys (Table II).⁴²

Although only collinear-spin configurations are studied in this work, the AFMD phase has been suggested to be a close approximation to a spin-spiral state.⁴¹ The minimum for the AFM1 state is only slightly higher in energy, but considerably smaller in volume. The more complete antiferromagnetic coupling in this phase favors smaller Fe-Fe distances and hence a smaller volume. The complexity increases even more with FM fcc Fe, where we obtain a low-spin (LS), low-volume minimum and a relatively higher-energy high-spin (HS), high-volume minimum. This is shown in greater detail in Fig. 2. The FM-LS fcc Fe has an equilibrium lattice parameter of 3.47 \AA and local magnetic moment of $0.95\mu_B$, while the FM-HS fcc Fe has an equilibrium lattice parameter of 3.64 \AA and a local magnetic moment of $2.62\mu_B$. As in the AFM Fe case, this lattice parameter agrees well with extrapolated values in FM fcc Fe alloys (3.65 \AA) at low temperature (Table II).

We find that the NM phase of fcc Fe is almost degenerate with the FM-LS phase. Experimentally, fcc Fe is found to be paramagnetic in the temperature range for which carbon dif-

TABLE II. PAW-DFT-GGA predictions of lattice parameters (a), bulk moduli (B), and local magnetic moments (M) for magnetic phases of bcc and fcc Fe at 0 K. Earlier FLAPW-DFT-GGA predictions and experimental measurements are also shown for comparison.

System	Method	a (Å)	B (GPa)	M (μ_B)
bcc FM	PAW ^a	2.83	174	2.20
	FLAPW ^b	2.84	174	2.17
	experiment	2.86 ^c	168 ^d	2.22 ^d
bcc NM	PAW	2.76	267	0.00
	FLAPW	2.77	279	0.00
bcc AFM1	PAW	2.79	166	1.22
	FLAPW	2.80	176	1.25
fcc FM HS	PAW	3.64	167	2.62
	FLAPW	3.64	171	2.57
fcc FM LS	PAW	3.47	214	0.94
	FLAPW	3.49	211	1.02
fcc FM	experiment	3.65 ^e		
fcc AFMD	PAW	3.52	130	1.79
	FLAPW	3.53	127	1.80
fcc AFM1	PAW	3.48	198	1.23
	FLAPW	3.50	193	1.30
fcc AFM	experiment	3.56 ^e		0.70 ^f
fcc NM	PAW	3.45	282	0.00
	FLAPW	3.46	293	0.00

^aAll the PAW data in this table are from the present work.

^bAll the FLAPW data in this table are from Ref. 40.

^cReference 42 (extrapolated to 0 K).

^dReference 31.

^eReference 42 (lattice parameters are derived by extrapolating those of fcc Fe alloys at 4 K to a pure Fe concentration).

^fReference 43 (the magnetic moment is measured for fcc Fe precipitates in the Cu matrix below T_N).

fusion has been observed (1000–1500 K). So which phase should be chosen to model austenite, given the various magnetic phases of fcc Fe? The NM phase is not a good choice because the paramagnetic state consists of randomly disordered local magnetic moments, but not in the sense of locally compensated spins as in our NM phase. Instead, we choose

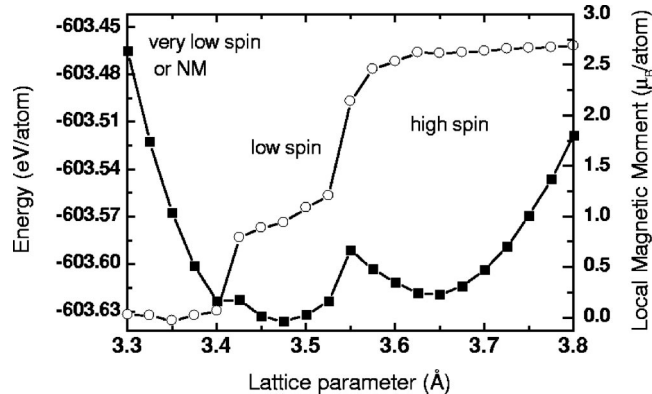


FIG. 2. Total energy (solid squares) and local magnetic moment (open circles) of FM fcc Fe as a function of lattice parameter.

TABLE III. Solution enthalpies (ΔH_s) of carbon in FM bcc Fe at 0 K for both unrelaxed and relaxed structures (for the unrelaxed structure, $a = 2.86$ Å) and the c/a ratio for the relaxed cells.

Supercell	ΔH_s , unrelaxed (eV)	ΔH_s , relaxed (eV)	c/a
Fe16C1	5.62	0.58	1.076
Fe54C1	5.60	0.72	1.019
Fe128C1	5.60	0.74	1.007

the FM-HS phase as our model system for austenite for the following reasons. First, the AFM (or the spin-spiral state) and the FM-HS phases of fcc Fe have been observed experimentally either from the precipitates of fcc Fe in a Cu matrix⁴⁷ or from fcc Fe thin films grown on a substrate,⁴⁸ while the FM-LS phase has not. Second, the FM-HS state of fcc Fe has been invoked as an excited state to explain the anti-Invar effect of fcc Fe.^{40,42} Though we cannot model the paramagnetic phase with conventional periodic DFT and collinear spins, we conclude that it is better to use the FM-HS phase to model austenite (again, the lattice parameter is similar to the extrapolated values in FM fcc Fe alloys) rather than the FM-LS, NM, or AFM phases of fcc Fe (which do not resemble a paramagnetic phase at all).

B. Solution enthalpy of carbon in FM bcc Fe

Although the nominal “radius” of the tetrahedral (t) site [0.36 Å, as measured from its center to the nearest Fe atom, minus the metallic radius of Fe (Ref. 49)] of the Fe bcc lattice is larger than that of the octahedral (o) site (0.19 Å), carbon prefers to stay in the o-site. Experimentalists have made this point,^{49,50} and we also confirm this with first-principles calculations using an Fe16 supercell. Insertion of C into bulk bcc Fe held rigid in its pure elemental structure yields a solution enthalpy ~ 1.00 eV less endothermic for the t-site than for the o-site, consistent with the larger size of the t-site. However, the order is reversed upon structural relaxation, with the o-site about 1.00 eV more stable than the t-site. Carbon atoms have covalent radii of 0.77 Å, so both the o-site and t-site may be considered far too small. However, carbon atoms prefer to stay in distorted octahedral sites, where they can have only two Fe atoms close to them upon relaxation, rather than four close Fe atoms in the tetrahedral sites. We therefore focus on calculating a converged solution enthalpy of carbon in the o-site.

Table III shows how the solution enthalpy of carbon in an Fe lattice converges with the supercell size, i.e., as the concentration of carbon becomes lower. The solution enthalpy in the structurally unrelaxed cell is very large (about 5.6 eV), which suggests that the dissolution of carbon in bcc Fe is very unfavorable. After relaxation, the solution enthalpy is reduced dramatically but is still significantly positive, which agrees with the low solubility of carbon in ferrite. With increasing dilution of C (increasing supercell size), one sees that the solution enthalpy is converged to ~ 0.73 eV at Fe54C1, since the numerical error in our calculations is estimated to be around 0.02 eV/cell. The calculated solution enthalpy agrees very well with the experimental value (0.60–0.78 eV) measured in the temperature range of 773–993 K.⁵¹

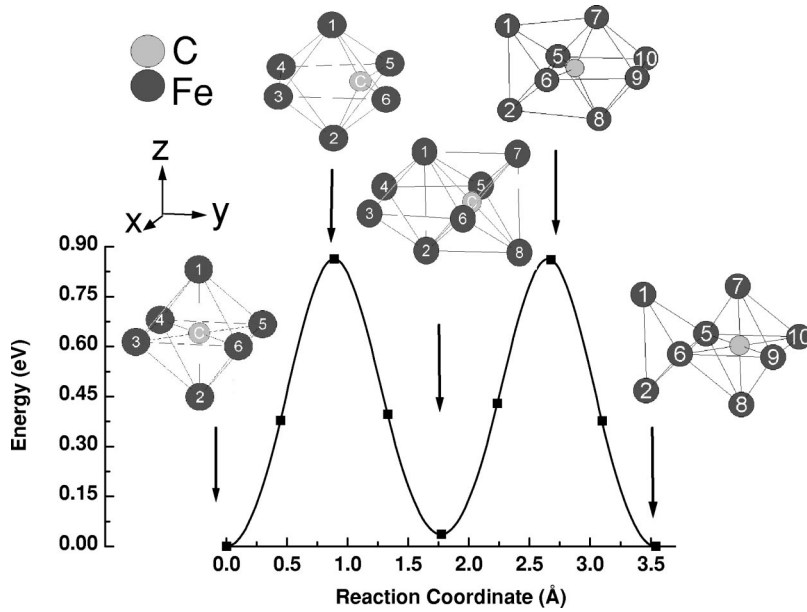


FIG. 3. Minimum-energy path for carbon diffusion in the Fe128C1 supercell and the local structures of initial, intermediate, final, and transition states.

From Fe16 to Fe54, the solution enthalpy for the relaxed structure increases by about 0.14 eV, which indicates a possible attractive interaction between carbon atoms in the bcc Fe lattice, whereby these carbon atoms may be driven to precipitate out from the bcc lattice. Experimentally, Fe₃C instead of graphite is formed upon tempering a supersaturated carbon solution in ferrite, due to kinetic reasons.³²

After relaxation, we find that the bcc lattice undergoes a tetragonal distortion and adopts a body-centered-tetragonal (bct) structure, with the c/a ratio of the bct structure decreasing with increasing cell size. We obtain a bct structure instead of the cubic lattice after relaxation of the supercell because of the strain caused by the carbon in the o-site of the periodic bcc lattice. In a real world sample, carbon atoms are randomly distributed in the o-sites of the bcc lattice, leading to a macroscopic cubic symmetry despite possible local tetragonal distortions (such distortions will average out along all three orientational variants, x , y and z). We conclude that the Fe128C1 supercell, with its very small tetragonal distortion, is sufficient to simulate carbon diffusion in ferrite, since the local coordination around the carbon atom in the bct structure is quite similar to ferrite.

C. Carbon diffusion in FM bcc Fe

The most likely and intuitive hopping mechanism for interstitial diffusion of carbon in the bcc lattice is the linear movement of the interstitial element from an o-site to another nearest neighbor one via the t-site. If the long axis (c axis) in our bct Fe128C1 supercell is along the z axis, then the carbon atom can diffuse in either the x or y direction (see Fig. 3). Suppose the carbon atom hops one step along the y direction to another nearest-neighbor o-site. Then the c axis of the tetragonal distortion will change to be along the x direction. If the carbon moves a further step along the y direction, then the c axis will change back to the z axis. Since the current implementation of the NEB method requires that the initial and final states have the same cell shape and vol-

ume, we take one o-site and its next-nearest-neighbor o-site along the y direction as the initial and final states, respectively. Thus the o-site in between becomes a local minimum which has a small tensile stress along the x direction, and causes its energy to be a little higher than the initial state. All this analysis is reflected in and confirmed by Fig. 3 (the discrete data points are connected with a cubic spline). The diffusion barrier is calculated to be 0.86 eV, which agrees beautifully with the experimental value of 0.87 eV.⁷ This result indicates that Fe128 is sufficiently large to simulate carbon diffusion in bcc Fe. The local minimum in the middle (image 04) is about 0.04-eV higher than the initial state (image 00), indicating that the tensile stress on image 04 is not large. The local structures of the initial state, the transition states (images 02 and 06), the local minimum, and the final state (image 08) are also shown in Fig. 3. One can see that the carbon atom moves from one octahedron to another one via the t-site as a transition state. The decrease of the Fe1-Fe2 distance and the increase of the Fe5-Fe6 distance also support this diffusion process (Table IV). So our calculations not only agree with the experimental barrier but also confirm that the mechanism assumed by experimentalists⁹⁻¹² is associated with this barrier.

In order to compare the diffusion coefficient with experiment, we also calculate the preexponential factor for carbon diffusion in bcc Fe. Using harmonic transition-state theory⁵² and the random-walk formulation of interstitial diffusion in a bcc lattice,⁵³ D_0 in the empirical Arrhenius form of the diffusion equation $D = D_0 \exp(-E_a/k_B T)$ can be expressed as

TABLE IV. The geometries of images 00, 02, and 04 of the Fe128C1 cell.

Image	Fe1-Fe2 (Å)	Fe5-Fe6 (Å)	C-Fe5 (Å)
00 (minimum)	3.559	2.797	1.978
02 (TS)	3.361	3.353	1.820
04 (strained minimum)	2.811	3.550	1.775

TABLE V. Solution enthalpies (ΔH_s) of carbon in FM-HS fcc Fe at 0 K for both unrelaxed and relaxed structures (for the unrelaxed structure, $a = 3.64$ Å) and the percent of change in volume (ΔV).

Supercell	ΔH_s , unrelaxed (eV)	ΔH_s , relaxed (eV)	ΔV (%) ^a
Fe4C1	0.38	-0.06	11.2
Fe32C1	0.33	-0.17	0.98
Fe64C1	0.33	-0.16	0.50
Fe125C1	0.34	-0.17	0.10

^aThe volume increase of the relaxed Fe_nC_1 cell with respect to the relaxed Fe_n cell.

$D_0 = \frac{1}{6} a^2 (\prod_{j=1}^{3N} \nu_j / \prod_{j=1}^{3N-1} \nu_j^\ddagger)$. Here, a is the lattice parameter, and ν_j and ν_j^\ddagger are the real normal-mode frequencies at the initial state and the transition state, respectively. By constructing and diagonalizing a small Hessian matrix which involves only C, Fe5, and Fe6 (Fig. 3), we obtain nine ν_j 's and eight ν_j^\ddagger 's (the other ν_j^\ddagger is imaginary), leading to a calculated $D_0 = 1.44 \times 10^{-7} \text{ m}^2 \text{ s}^{-1}$. Experimental D_0 's vary by about one order of magnitude; the average over all available experimental data below 350 K (Ref. 54) gives a D_0 of $1.67 \times 10^{-7} \text{ m}^2 \text{ s}^{-1}$. Therefore, both our activation energy E_a and preexponential factor D_0 agree very well with experiment for carbon diffusion in FM bcc Fe. This gives us confidence to then apply a similar strategy to predict carbon dissolution and diffusion behavior in the less well-characterized fcc Fe (austenite).

D. Solution enthalpy of carbon in HS-FM fcc Fe

Experiments show^{15,16} that interstitial carbon stays predominantly in the octahedral sites of the fcc Fe lattice. This agrees with the larger “radius” of the o-site (0.53 Å) relative to the t-site (0.29 Å) in the fcc Fe lattice. We therefore build all the supercells with carbon in an octahedral interstitial site and with a lattice parameter of 3.64 Å, which we obtain as the equilibrium lattice parameter for the unit cell of FM-HS fcc Fe. The solution enthalpies for the unrelaxed and relaxed cell structures are converged at the supercell size of Fe32C1 (Table V). The negative sign and small magnitude of the solution enthalpy for the fully relaxed structures show that the dissolution of carbon atoms in FM-HS fcc Fe is slightly exothermic and, in fact, is energetically favorable even for such high carbon concentrations as represented by as small a cell as Fe4C1. This is partly due to the relatively large atomic volume of FM-HS fcc Fe.

For comparison, we also calculated the solution enthalpy of carbon in the t-site for the Fe32C1 cell and we find it is about 1.48 eV higher for the relaxed structure (and 4.33 eV higher for the unrelaxed structure) than for C in the o-site, confirming the experimental observation that C prefers the o-site.

The decrease in the solution enthalpy for the relaxed structures, going from Fe4C1 to Fe32C1, can be explained by a repulsive interaction between the carbon atom and its periodic images for the Fe4C1 cell. Experimental evidence exists to support the idea that C-C interactions here are re-

pulsive. The interaction between interstitial carbon atoms in fcc Fe was estimated experimentally by measuring the concentration dependence of carbon activity, and it was deduced that the interaction is repulsive between carbon atoms in austenite.⁵⁵ Moreover, Mössbauer spectra of austenite have also been interpreted in terms of a repulsive carbon-carbon pair interaction, based on a Monte Carlo simulation analysis.⁵⁶

It is evident from Table V that the volume expansion (ΔV) decreases as the cell becomes larger and is about 1% for Fe32C1. If the solution enthalpy is taken as a criterion for the cell convergence, then Fe32C1 is large enough for our study. This supercell is much smaller than the converged supercell for bcc Fe (Fe128C1). In the latter phase, carbon, in the o-site of bcc Fe, has a larger strain field, causing a significant tetragonal distortion to the lattice (the energy gain from structural relaxation is large, ~ 5.0 eV). So it takes a much larger cell to minimize the interactions between the strain fields caused by carbon and its periodic images in bcc Fe. On the other hand, both the strain field and the lattice distortion caused by carbon in the o-site of fcc Fe have octahedral symmetry and are isotropic, and the energy gain from the structural relaxation is small, ~ 0.50 eV. Thus the smaller distortions caused by C in fcc Fe allow us to converge the results with a much smaller cell than in bcc Fe. These findings are consistent with the low solubility of carbon in bcc Fe compared to fcc Fe, as mentioned in the Introduction.

In the following, we examine carbon diffusion in the Fe32 supercell in order to simulate the dilute concentrations present in most austenitic studies. For comparison, however, we also investigate carbon diffusion in the Fe4 cell as a model of a supersaturated solution of carbon in Fe.

E. Diffusion of supersaturated carbon in FM-HS fcc Fe: The Fe4C1 cell

For interstitial carbon in fcc Fe, we consider only the diffusion of carbon from an o-site to another nearest-neighbor o-site. In the conventional cubic fcc cell, the carbon moves from the edge center (0.0, 0.0, 0.5) to the body center (0.5, 0.5, 0.5). Figure 4 shows the converged MEP and the atomic arrangements of images 00, 06, 08, and 16 that represent the initial state, the first transition state, the intermediate state, and the final state, respectively. One can see that the MEP shows a symmetric structure with double maxima at 2.10 eV and one t-site intermediate at 2.05 eV. The geometries of images 00, 06, and 08 are shown in Table VI. In the initial state, the carbon atom is in the octahedron that includes Fe1, Fe2, and Fe3. In the transition state, the carbon atom is approximately in the center of the triangle of Fe1, Fe2, and Fe3. For the intermediate, the carbon atom is approximately at the center of the tetrahedron that consists of Fe1, Fe2, Fe3, and Fe4; this can be seen from the fairly tetrahedral Fe1-C-Fe2 and Fe2-C-Fe3 angles ($\sim 109.4^\circ$). The carbon atom then will move to the second transition state that is at the center of the triangle of Fe2, Fe3, and Fe4, and then arrives at the final state—the (octahedral) body center. The transition-state image has the shortest Fe-C distance

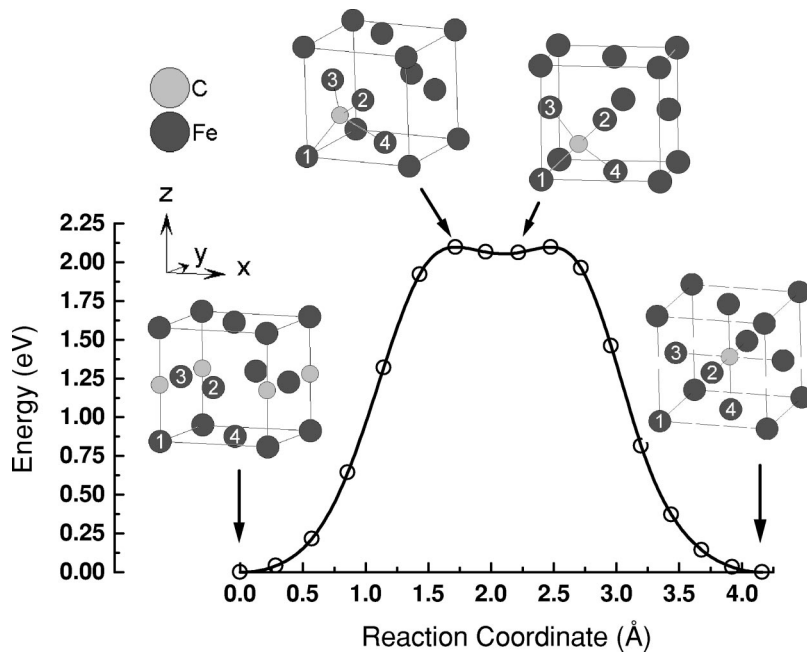


FIG. 4. Minimum-energy path for carbon diffusion in the fcc Fe₄C₁ supercell and the structures of the initial state, the first transition state, the intermediate state, and the final state.

of ~ 1.75 Å. The t-site is an intermediate for carbon diffusion between o-sites, but the energy well is very shallow, only about 0.05 eV lower than the transition state. The diffusion mechanism that we find for Fe₄C₁ is close to what most experimentalists have conjectured about interstitial diffusion in an fcc lattice.^{57,58} Namely, instead of going directly from one o-site to another nearest one within the (001) plane by pushing two atoms apart, the interstitial moves off plane and goes through a curved channel connecting the two o-sites, as shown in Fig. 4.

F. Diffusion of dilute carbon in FM-HS fcc Fe: The Fe₃2C₁ cell

From the solution enthalpy convergence tests (Table V), we see that a Fe₃2C₁ supercell is suitable to simulate isolated carbon interstitials in fcc Fe. The converged MEP (Fig. 5) shows a symmetrical path with a high-energy plateau and a diffusion barrier of 0.99 eV. The middle point of the MEP is found to be a local minimum of 0.98 eV, which is only about 0.01-eV lower in energy than the two transition states. So just as in the Fe₄C₁ cell, the MEP of the Fe₃2C₁ system also has a symmetrical double maxima and an intermediate in between, although the well is much shallower than that of Fe₄C₁. Also shown in Fig. 5 are the structures of images 00, 04, 06, 07, and 12, which correspond to the initial state, the first transition state, the intermediate, the second transition

state, and the final state, respectively. One can see that the carbon atom pushes away Fe₂ and Fe₃ and goes almost linearly from the initial o-site to the final one. Unlike Fe₄C₁, in which the carbon atom moves off plane and through a t-site intermediate, the carbon atom in Fe₃2C₁ basically stays in the (001) plane containing the carbon, Fe₂, and Fe₃, avoiding the t-site! The very similar Fe₂-C distances (Table VII) of images 04, 06, and 07 (1.773–1.776 Å) explain why there is a plateau in the MEP. For image 06 (the intermediate), the carbon is nearly perfectly collinear and in between Fe₂ and Fe₃ (179.6°), and no tetrahedral angle is found there. The apparent discrepancy between the lower energy of image 06 and its shorter C-Fe₂ distance compared with image 04 can partly be explained by the shorter C-Fe₄ and C-Fe₆ distances in image 06, producing slightly better coordination than image 04 and therefore a lower energy.

Normally, the NEB method converges the chain of images to the MEP that is closest to the initial guess, so it depends on how the initial interpolation is done. To see whether there is an MEP going through the t-site, we also did a CI-NEB run with a “nonlinear” interpolation which included the t-site in the initial guess. The chain of images converges again to the same MEP we obtained above from the linear interpolation, indicating that there is no saddle point going through the t-site for dilute carbon concentrations in fcc Fe.

Another concern with the NEB method is that the current implementation works only with fixed volume along the

TABLE VI. The geometries of images 00, 06, and 08 for the Fe₄C₁ cell.

Image	Distance (Å)				Angle (°)	
	C-Fe1	C-Fe2	C-Fe3	C-Fe4	Fe1-C-Fe2	Fe2-C-Fe3
00 (minimum)	1.882	1.882	1.882	3.260	90.0	90.0
06 (TS)	1.753	1.751	1.751	1.914	117.9	118.4
08 (intermediate t-site)	1.785	1.774	1.774	1.770	107.9	110.3

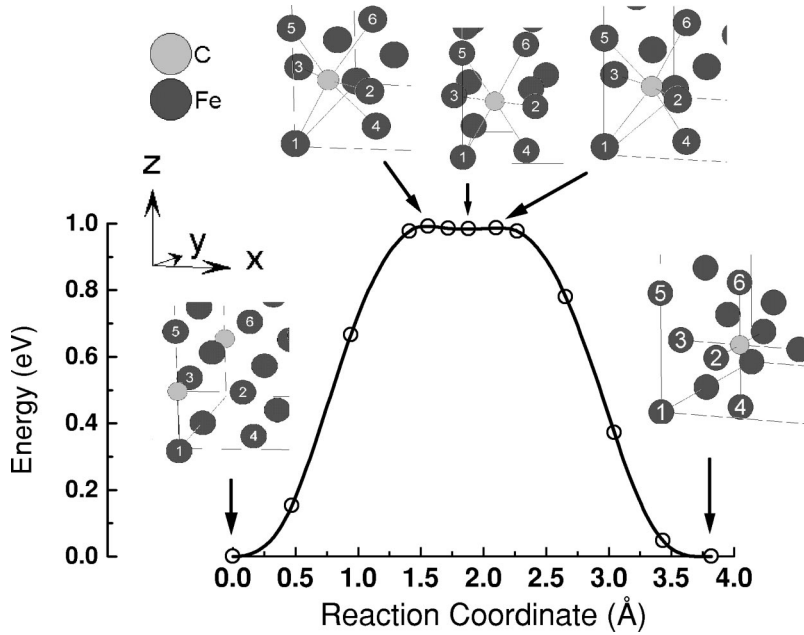


FIG. 5. Minimum-energy path for carbon diffusion in the Fe_{32}C_1 supercell and the local structures of the initial state, the first transition state, the intermediate state, the second transition state, and the final state.

path. In order to assess whether the constant volume constraint introduces significant stress along the diffusion path, we compared the structure of the TS with that of the initial state to see how the average Fe-Fe distance changes moving away from the C atom. If the distance converges to the pure Fe value within half of the simulation cell dimension, then the perturbation due to the diffusing carbon is short ranged and no stress will be accumulated due to this constraint. In Fig. 6, we see that the Fe-Fe distance for the initial state converges to about 2.565 \AA (very near that of pure Fe, shown as the dotted horizontal line) near 3.6 \AA , which is half of the supercell lattice parameter. Therefore, no stress buildup is present in this simulation cell for the initial state. However, the transition-state Fe-Fe distances are still oscillating around that of the initial state with an amplitude of $\sim 0.02 \text{ \AA}$ for the Fe-C distances larger than half the simulation box length. Although this amplitude is small, it indicates there is some small stress for the TS configuration. We expect this amplitude would decrease if a larger supercell was used, which would decrease the activation energy slightly if this was accounted for.

IV. DISCUSSION

Comparisons of first-principles predictions with experimental measurements must be undertaken very carefully. Seemingly identical phenomena studied by simulation and

by experiment often turn out to be quite different. In some sense, first-principles studies are more like an ideal lab in which a simplified material is used to model a more complicated real world material. In this section, we compare our model predictions with real materials and try to relate our findings in a relevant way to previous experiments.

A. Zero-point energy corrections and thermal effects on the energetics of dissolution and diffusion

Experimental data, of course, include the effect of zero-point energy (ZPE), while most condensed-matter calculations do not. However, ZPE corrections can be added afterwards in order to compare directly with experiments, if the experimental data can be extrapolated to 0 K. ZPE corrections, in principle, can be important for light elements, while they are more or less negligible for heavy elements. By obtaining the normal-mode frequencies of carbon in either graphite or the bcc Fe lattice, we can estimate the effect of carbon's ZPE on the energetics we have calculated. In this way, the ZPE of graphite is estimated to be 0.13 eV/atom . Keeping the Fe atoms rigid (i.e., assuming infinite mass) at their equilibrium positions, the ZPE of carbon in the o-site of bcc Fe (for the $\text{Fe}_{128}\text{C}_1$ cell) is estimated to be 0.11 eV/atom . These give a correction of -0.02 eV to the solution enthalpy for carbon in bcc Fe. The ZPE of carbon at the transition state for carbon diffusion in bcc Fe is estimated to

TABLE VII. The geometries of images 00, 04, 06, 07, and 12 for the Fe_{32}C_1 cell.

Image	Distance (\AA)						Angle ($^\circ$)	
	C-Fe1	C-Fe2	C-Fe3	C-Fe4	C-Fe5	C-Fe6	Fe1-C-Fe2	Fe2-C-Fe3
00 (minimum)	1.903	1.903	1.903	3.156	1.903	1.903	90.0	90.0
04 (first TS)	2.003	1.776	1.776	2.121	2.005	2.107	92.6	168.2
06 (local minimum)	2.042	1.773	1.772	2.043	2.043	2.037	89.6	179.6
07 (second TS)	2.115	1.776	1.776	2.006	2.109	2.007	85.7	168.8

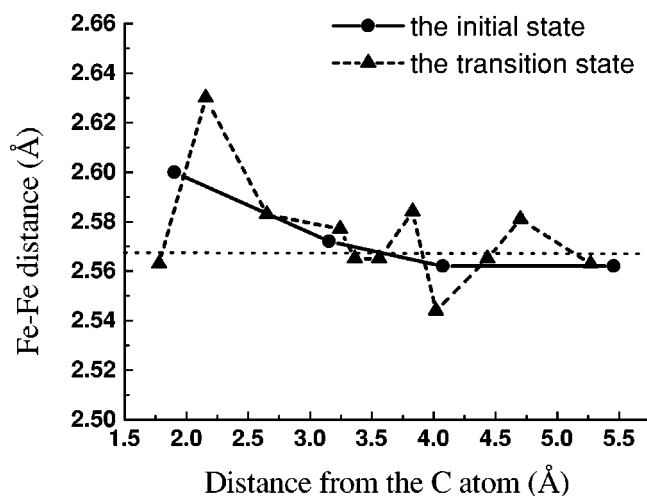


FIG. 6. Average Fe-Fe distance versus distance from the carbon atom in the Fe₃₂C₁ cell.

be 0.08 eV, which produces a correction of -0.03 eV to the diffusion barrier. Since the ZPE corrections for carbon in bcc Fe are about at the numerical error in our calculations, we conclude they can be neglected and therefore did not estimate them for carbon in fcc Fe.

In principle, thermal effects also should be considered when comparing first-principles energetics (usually at 0 K) with experiment (always at finite temperature). For example, the experimental solution enthalpy of C in bcc Fe is measured in the temperature range of 773–993 K.⁵¹ However, since thermal corrections (due to differential changes in heat capacities from initial to final states) are typically as small as and of opposite sign to ZPE corrections, we have not attempted to include them in our calculations. We therefore directly compare experimental finite temperature energetics to non-ZPE-corrected, 0-K theoretical energetics, noting the likelihood of a fortuitous cancellation of (small) errors.

B. Are we simulating diffusion in ferrite or martensite?

The bct structure we obtain after relaxing the bcc Fe-C supercell as a model of ferrite is different from the bct structure of martensite, which is experimentally obtained from a diffusionless martensitic transformation by quenching austenite (fcc Fe). The structure of martensite is metastable, and it will decompose to ferrite (bcc Fe) and cementite (Fe₃C) upon tempering.⁵⁹ The bct structure we obtain is the theoretical ground state of the Fe-C alloy, although it is supersaturated with C (~ 0.17 wt % C for Fe₁₂₈C₁) compared with the experimental phase diagram, where saturation occurs at 0.02 wt % C at 1000 K (at lower temperatures, the solubility will be even lower⁶⁰). If we restrict the supercell to retain bcc symmetry, we find this to be higher in energy than the bct structure. For example, we did a calculation for the Fe₁₆C₁ cell, with a uniformly expanded lattice, and with carbon in the o-site and Fe atoms fixed at their bcc lattice positions. We found that the uniformly expanded bcc lattice at its lowest energy is still 4.20-eV higher in energy than the relaxed Fe₁₆C₁ cell. So the bct structure we obtained is indeed the ground state of the Fe-C alloy at this C concentration.

The local structure of carbon in the lattice also shows that our bct structure is different from martensite. X-ray diffraction shows⁶¹ that the distances between C and the six Fe atoms of its first coordination shell in martensite are almost the same at 1.93 Å. This means that the coordination octahedron of carbon (and therefore, the local environment of carbon) in martensite is almost the same as that in the austenite. However, for our relaxed Fe₁₂₈C₁ cell, the C atom is about 0.20-Å closer to the two Fe atoms along the *c* axis than to the four Fe atoms on the *a-b* plane, which indicates that the local environment of carbon is more ferritelike. We therefore consider that our bct structure is a close model of bcc Fe with supersaturated carbon, which is different from the metastable bct structure of martensite. The (fortuitously) perfect agreement of the diffusion barrier with the experimental value of carbon diffusion in ferrite also supports this point.

C. How do we compare with experiments for diffusion in austenite?

Our diffusion predictions for carbon in austenite unfortunately are not directly comparable to experiments. The diffusion experiments are usually done at high temperatures where austenite is stable and paramagnetic. Since we cannot simulate paramagnetic Fe with conventional DFT and there is no experimental information on local magnetic moments in Fe-C alloys,⁶² we chose to use the FM-HS state of Fe to simulate austenite, as explained earlier. The complicated magnetovolume instability of fcc Fe makes it difficult for any first-principles method to accurately describe austenite. It should be noted also that calculations suggest⁶³ that FM-HS fcc Fe is not stable under tetragonal distortion. In our study, however, all the fcc cells were constrained to be cubic. Keeping these points in mind, we now attempt to make some comparison with experiment.

We predicted the diffusion barrier for carbon in austenite to be 0.99 eV, which is about 0.60-eV lower than the experimental value.¹⁴ In order to obtain another limiting value, we calculated the diffusion barrier for carbon in NM fcc Fe. The result is ~ 2.70 eV, which is far too high and indicates that the NM state is not suitable for describing austenite. We then attempted a similar calculation for the FM-LS phase of fcc Fe. Unfortunately, the FM-LS phase becomes unstable after a C atom is put into the lattice, and it relaxes to the NM phase. We have not tried to use the AFM phases of Fe to study carbon diffusion.

So how can we connect our predicted value to measurements? The excellent agreement with experiment for the diffusion barrier for carbon in bcc Fe suggests that we can consider our barrier for carbon diffusion in FM-HS fcc Fe to be an accurate prediction of the barrier when such a phase of Fe exists. Thin films of FM-HS fcc Fe can be obtained by the deposition of thin layers of Fe on Cu(100) substrates.^{64–67} When the number of layers in the film exceeds 11 monolayers, the fcc structure usually becomes unstable and transforms to the bcc structure.^{64,68} However, Kirilyuk *et al.* have shown⁶⁹ that fcc Fe films with up to 60 monolayers can be produced by the cooperative surfactant effect of carbon and oxygen. They admit to the vacuum chamber gases such as

C_2H_2 , C_2H_4 , and CO as carbon sources and O_2 as the oxygen source during molecular-beam epitaxy. They believe that the main reason they are able to stabilize the fcc structure is the interstitial incorporation of carbon atoms into the fcc lattice. This observation is consistent with our predicted solution enthalpy of carbon in fcc FM-HS Fe, which shows that the dissolution of carbon into the bulk is energetically favorable. If the diffusion barrier could be measured experimentally in such a situation, then a direct comparison to our prediction could be made.

V. SUMMARY

We performed periodic DFT calculations of the dissolution and diffusion energetics for interstitial carbon in bcc and fcc Fe. We find that for ferromagnetic (FM) bcc Fe, the stable phase at low temperature places carbon in the octahedral site. The solution enthalpy of carbon in the octahedral site is predicted to be 0.74 eV endothermic, consistent with the very small solubility of C in bcc Fe. Simulation cell size convergence tests demonstrate that an Fe128 supercell is sufficient to simulate the energetics of the interstitial carbon in FM bcc Fe. The minimum-energy path (MEP) of carbon diffusion with a supercell of Fe128C1 gives a diffusion barrier of 0.86 eV, in excellent agreement with experiment. The tetrahedral site is found to be a transition state (TS), as postulated previously.^{9,10}

Despite the magnetovolume instability of fcc Fe, the all-electron PAW-DFT-GGA method provides descriptions of the antiferromagnetic single-layer (AFM1), antiferromagnetic double-layer (AFMD), nonmagnetic (NM), ferromagnetic low-spin (FM-LS), and ferromagnetic high-spin (FM-HS) states of fcc Fe that agree very well with earlier all-electron FLAPW-DFT-GGA results. Given the known paramagnetism of austenite, which cannot be easily modeled within conventional DFT, we chose to model austenite with the ferromagnetic high-spin phase of fcc Fe as the phase closest to a paramagnetic phase.

Our predicted solution enthalpy indicates that the dissolution of carbon in FM-HS fcc Fe is slightly exothermic. Simulation cell size convergence tests indicate that an Fe32 supercell is sufficient to simulate the dissolution energetics of the interstitial carbon in FM-HS fcc Fe. We also find repulsive

interactions between carbon atoms at high concentrations, consistent with experimental observation.^{55,56} This is in direct contrast to the attraction predicted between carbon atoms in bcc Fe, consistent with the tendency of carbon to precipitate out as Fe_3C in bcc Fe.

The MEP of carbon diffusion in an fcc Fe4C1 cell (supersaturated solution of C in fcc Fe) shows double maxima with a diffusion barrier of 2.10 eV and one intermediate of 2.05 eV. The carbon atom moves from an initial octahedral site through the center of a Fe triangle (a transition state), then to a tetrahedral site (an intermediate), then another center of a Fe triangle (a second transition state), and finally to another octahedral site. This mechanism of interstitial diffusion in the fcc lattice is the most intuitive and has been employed to explain measurements.^{57,58}

The diffusion of carbon at lower concentrations in an fcc Fe32C1 cell shows a totally different MEP. The carbon atom takes a shortcut between two neighboring octahedral sites and moves linearly from the initial state to the final state by pushing away two Fe atoms in the way. This offers a new way of thinking about the diffusion of light interstitials in the fcc lattice. Although we have not yet studied other systems to prove this is a general mechanism, this possible diffusion path should be kept in mind when interpreting experimental data. The barrier predicted for this pathway is 0.99 eV. We suggest that this value might be able to be confirmed experimentally by measuring carbon diffusion in a thick enough fcc Fe film with FM order, which could be grown on a Cu(100) substrate.^{67,69}

ACKNOWLEDGMENTS

We thank the Army Research Office for funding this research, the Maui High Performance Computing Center, and the NAVO MSRC for CPU time. We thank Professor Hannes Jónsson for his CI-NEB and dynamical matrix modules. D.E.J. thanks Dr. Georg Kress for suggesting the PAW method for the Fe system. D.E.J. is very grateful to Dr. Graeme Henkelman for his answers and suggestions for using CI-NEB. D.E.J. thanks Professors Wolfgang Windl and Otto F. Sankey for the program “DYNMAT.” We thank Ms. Karin Carling and Dr. Kyle Caspersen for helpful discussions.

¹M.C. Payne, M.P. Teter, D.C. Allan, T.A. Arias, and J.D. Joannopoulos, *Rev. Mod. Phys.* **64**, 1045 (1992).

²J. Hafner, *Acta Mater.* **48**, 71 (2000).

³W. Windl, M.M. Bunea, R. Stumpf, S.T. Dunham, and M.P. Masquelier, *Phys. Rev. Lett.* **83**, 4345 (1999).

⁴B.P. Uberuaga, M. Leskovaar, A.P. Smith, H. Jónsson, and M. Olmstead, *Phys. Rev. Lett.* **84**, 2441 (2000).

⁵N. Sandberg, B. Magyari-Köpe, and T.R. Mattsson, *Phys. Rev. Lett.* **89**, 065901 (2002).

⁶R.J. Needs, *J. Phys.: Condens. Matter* **11**, 10 437 (1999).

⁷C.A. Wert, *Phys. Rev.* **79**, 601 (1950).

⁸Y. Iijima, *J. Alloys Compd.* **234**, 290 (1996), and references

therein.

⁹J.L. Snoek, *Physica (Amsterdam)* **8**, 711 (1941).

¹⁰D. N. Beshers, *Diffusion in Body-Centered Cubic Metals* (American Society for Metals, Metals Park, OH, 1965), p. 149.

¹¹R.H. Condit and D.N. Beshers, *Trans. Metall. Soc. AIME* **239**, 680 (1967).

¹²R.B. McLellan, M.L. Rudee, and T. Ishibachi, *Trans. Metall. Soc. AIME* **233**, 1938 (1965).

¹³C. Wells, W. Batz, and R.F. Mehl, *Trans. AIME* **188**, 553 (1950).

¹⁴R.P. Smith, *Trans. Metall. Soc. AIME* **230**, 476 (1964).

¹⁵B.D. Butler and J.B. Cohen, *Ultramicroscopy* **52**, 238 (1993).

¹⁶B.D. Butler and J.B. Cohen, *J. Phys. I* **2**, 1059 (1992).

- ¹⁷P. Hohenberg and W. Kohn, Phys. Rev. **136**, B864 (1964).
- ¹⁸W. Kohn and L.J. Sham, Phys. Rev. **140**, A1133 (1965).
- ¹⁹G. Kresse and J. Hafner, Phys. Rev. B **48**, 13 115 (1993).
- ²⁰G. Kresse and J. Furthmüller, Phys. Rev. B **54**, 11 169 (1996).
- ²¹G. Kresse and J. Furthmüller, Comput. Mater. Sci. **6**, 15 (1996).
- ²²P.E. Blöchl, Phys. Rev. B **50**, 17 953 (1994).
- ²³G. Kresse and D. Joubert, Phys. Rev. B **59**, 1758 (1999).
- ²⁴D. E. Jiang, E. A. A. Jarvis, and E. A. Carter (unpublished).
- ²⁵D.J. Singh, W.E. Pickett, and H. Krakauer, Phys. Rev. B **43**, 11 628 (1991).
- ²⁶J.P. Perdew, J.A. Chevary, S.H. Vosko, K.A. Jackson, M.R. Pederson, D.J. Singh, and C. Fiolhais, Phys. Rev. B **46**, 6671 (1992).
- ²⁷S.H. Vosko, L. Wilk, and M. Nusair, Can. J. Phys. **58**, 1200 (1980).
- ²⁸H.J. Monkhorst and J.D. Pack, Phys. Rev. B **13**, 5188 (1976).
- ²⁹F.D. Murnaghan, Proc. Natl. Acad. Sci. U.S.A. **30**, 2344 (1944).
- ³⁰A. Ludstsch, Acta Crystallogr., Sect. A: Cryst. Phys., Diffraction, Theor. Gen. Crystallogr. **28**, 59 (1972).
- ³¹C. Kittel, *Introduction to Solid State Physics*, 7th ed. (Wiley, New York, 1996).
- ³²W. D. Callister, Jr., *Materials Science and Engineering: An Introduction*, 5th ed. (Wiley, New York, 2000).
- ³³H.J.F. Jansen and A.J. Freeman, Phys. Rev. B **35**, 8207 (1987).
- ³⁴G. Henkelman, B.P. Uberuaga, and H. Jónsson, J. Chem. Phys. **113**, 9901 (2000).
- ³⁵H. Jónsson, G. Mills, and K. W. Jacobsen, in *Classical and Quantum Dynamics in Condensed Phase Simulations*, edited by B. J. Berne, G. Ciccotti, and D. F. Coker (World Scientific, Singapore, 1998), p. 385.
- ³⁶R.G. Della Valle and H.C. Andersen, J. Chem. Phys. **97**, 2682 (1992).
- ³⁷V.L. Moruzzi, P.M. Marcus, K. Schwarz, and P. Mohn, Phys. Rev. B **34**, 1784 (1986).
- ³⁸V.L. Moruzzi, P.M. Marcus, and J. Kübler, Phys. Rev. B **39**, 6957 (1989).
- ³⁹E.G. Moroni, G. Kresse, J. Hafner, and J. Furthmüller, Phys. Rev. B **56**, 15 629 (1997).
- ⁴⁰H.C. Herper, E. Hoffmann, and P. Entel, Phys. Rev. B **60**, 3839 (1999).
- ⁴¹D. Spišák and J. Hafner, Phys. Rev. B **61**, 16 129 (2000).
- ⁴²M. Acet, H. Zähres, E.F. Wassermann, and W. Pepperhoff, Phys. Rev. B **49**, 6012 (1994).
- ⁴³S.C. Abrahams, L. Guttman, and J.S. Kasper, Phys. Rev. **127**, 2052 (1962).
- ⁴⁴Y. Tsunoda, J. Phys.: Condens. Matter **1**, 10 427 (1989).
- ⁴⁵O.N. Mryasov, A.I. Liechtenstein, L.M. Sandratskii, and V.A. Gubanov, J. Phys.: Condens. Matter **3**, 7683 (1991).
- ⁴⁶M. Körling and J. Ergon, Phys. Rev. B **54**, R8293 (1996).
- ⁴⁷W. Keune, T. Ezawa, W.A.A. Macedo, U. Glos, K.P. Schletz, and U. Kirschbaum, Physica B **161**, 269 (1989).
- ⁴⁸C. Carbone, G.S. Sohal, E. Kisker, and E.F. Wassermann, J. Appl. Phys. **63**, 3499 (1988).
- ⁴⁹W. C. Leslie, *The Physical Metallurgy of Steels* (TechBooks, Herndon, VA, 1991), p. 68.
- ⁵⁰D.H. Jack and K.H. Jack, Mater. Sci. Eng. **11**, 1 (1973).
- ⁵¹M.A. Shumilov, A.P. Kozak, L.I. Yakushechikina, and K.N. Sokolov, Zh. Fiz. Khim. **47**, 2169 (1973).
- ⁵²G.H. Vineyard, J. Phys. Chem. Solids **3**, 121 (1957).
- ⁵³C. Wert and C. Zener, Phys. Rev. **76**, 1169 (1949).
- ⁵⁴J.R.G. da Silva and R.B. McLellan, Mater. Sci. Eng. **26**, 83 (1976).
- ⁵⁵R.B. McLellan and C. Ko, Acta Metall. **35**, 2151 (1987).
- ⁵⁶A.L. Sozinov, A.G. Balanyuk, and V.G. Gavriljuk, Acta Mater. **45**, 225 (1997).
- ⁵⁷G. Mah and C. Wert, Trans. Metall. Soc. AIME **230**, 16 (1964).
- ⁵⁸P. Shewmon, *Diffusion in Solids* (The Minerals, Metals, and Materials Society, Warrendale, PA, 1989), p. 56.
- ⁵⁹W. C. Leslie, *The Physical Metallurgy of Steels* (TechBooks, Herndon, VA, 1991), p. 226.
- ⁶⁰J.L. Bonnentien and J. Bigot, Mater. Trans., JIM **41**, 78 (2000).
- ⁶¹S.C. Moss, Acta Metall. **15**, 1815 (1967).
- ⁶²A.N. Timoshevskii, V.A. Timoshevskii, and B.Z. Yanchitsky, J. Phys.: Condens. Matter **13**, 1051 (2001).
- ⁶³P.M. Marcus, V.L. Moruzzi, and S.-L. Qiu, Phys. Rev. B **60**, 369 (1999).
- ⁶⁴J. Thomassen, F. May, B. Feldmann, M. Wuttig, and H. Ibach, Phys. Rev. Lett. **69**, 3831 (1992).
- ⁶⁵Th. Detzel, M. Vonbank, M. Donath, and V. Dose, J. Magn. Magn. Mater. **147**, L1 (1995).
- ⁶⁶W.A.A. Macedo and W. Keune, Phys. Rev. Lett. **61**, 475 (1988).
- ⁶⁷H. Jenniches, J. Shen, Ch.V. Mohan, S. Sundar Manoharan, J. Barthel, P. Ohresser, M. Klaua, and J. Kirschner, Phys. Rev. B **59**, 1196 (1999).
- ⁶⁸N. Memmel and Th. Detzel, Surf. Sci. **307**, 490 (1994).
- ⁶⁹A. Kirilyuk, J. Giergiel, J. Shen, M. Straub, and J. Kirschner, Phys. Rev. B **54**, 1050 (1996).